

Ultrafast and Directional Magnetization Control via Voltage-Controlled Exchange Coupling

Qi Jia¹, Yu-Chia Chen¹, Delin Zhang¹, Yang Lv¹, Shuang Liang², Onri Jay Benally¹, Yifei Yang¹, Brahm Dutta Dixit¹, Deyuan Lyu¹, Brandon Zink^{1,3} and Jian-Ping Wang^{*1}

¹ Department of Electrical and Computer Engineering Department, University of Minnesota, Minneapolis, MN, USA. ²Department of Chemical Engineering and Materials Science, University of Minnesota, Minneapolis, MN, USA. ³Present address: National Institute of Standards and Technology, Gaithersburg, MD USA

* e-mail: jpwang@umn.edu

Abstract

Ultrafast and energy-efficient electrically controlled magnetization switching is critical for next-generation spintronic devices. Voltage-driven switching offers an alternative to current-driven methods, significantly improving energy efficiency. Although voltage-controlled exchange coupling (VCEC) has been proposed to switch magnetic states, its ultrafast response has not been experimentally verified. Here, we demonstrate that VCEC induces a directional exchange field that persists under nanosecond voltage pulses in a perpendicular magnetic tunnel junction (pMTJ) with an exchange-coupled free layer. This establishes that VCEC can operate on ultrafast timescales with deterministic control over the switching polarity. The magnetization reversal is primarily assisted by voltage-induced magnetic anisotropy (VCMA), which transiently lowers the energy barrier. This combination enables magnetization switching within 87.5 ps with a 50% switching probability. The fast switching is attributed to enhanced magnetic relaxation of the free layer, facilitated by the exchange-coupled structure, which accelerates voltage-driven magnetization switching. These findings reveal that purely voltage-driven switching is viable for fast, bidirectional magnetization switching for future spintronic logic and memory technologies.

Main

Achieving energy-efficient and high-speed magnetization switching is critical for enabling next-generation spintronic logic and memory technologies¹⁻⁵. Current-induced magnetization switching, including spin-transfer torque (STT) and spin-orbit torque (SOT) mechanisms, has been extensively explored for magnetic random access memory (MRAM) applications⁶⁻⁹. However, these approaches inherently rely on high charge current densities ($>10^6$ A/cm²), stemming from the limited spin polarization of injected currents in STT or the limited spin conversion efficiency in SOT mechanisms, thereby hindering further improvements in switching performance and energy efficiency. In particular, the limited STT efficiency typically results in one nanosecond incubation delay during switching, undermining ultrafast magnetization reversal¹⁰⁻¹⁵. Although strategies such as incorporating a double polarizer or introducing a non-collinear spin polarizer have been proposed to reduce this delay to below 250 ps, they fundamentally fail to overcome the reliance on high charge current densities or can lead to non-deterministic switching behavior¹⁶⁻²⁰. Spin-orbit torque (SOT) switching offers advantages by reducing the incubation time, but it still demands high charge current density, often necessitates external field assistance for deterministic switching, and exhibits post-pulse switching²¹⁻²⁸. In addition, the three-terminal device geometry required for SOT increases the device footprint, posing challenges for high-density integration.

To address the energy and speed bottlenecks of current-driven switching mechanisms, voltage-controlled switching strategies have attracted growing interest. One representative example is voltage-controlled magnetic anisotropy (VCMA), which reduces switching energy by modulating magnetic perpendicular interfacial anisotropy (PMA). However, it typically requires an additional external magnetic field or current to achieve deterministic bipolar switching²⁹⁻³⁵. Beyond VCMA, another voltage-controlled mechanism, voltage-controlled exchange coupling (VCEC), offers a fundamentally different approach by tuning the interlayer exchange interaction between magnetic layers by an electric field. It enables deterministic bipolar switching without the need for large current density. Early demonstrations of voltage-tunable coupling relied on magneto-ionic effects driven by ionic motion, which raised concerns regarding switching speed and device endurance^{36,37}. In contrast, Bruno theoretically proposed an electronic mechanism for controlling exchange coupling through spin-dependent interfacial reflectivity³⁸. This mechanism was later experimentally demonstrated in MgO-based systems³⁹⁻⁴⁴, representing a voltage-driven alternative to STT switching in two-terminal MTJ devices⁴⁵. However, the VCEC effect has only been demonstrated under quasi-static conditions so far, and its applicability for nanosecond, deterministic switching remains an open question.

In this work, we design, deposit, and pattern a multilayer FM₁/NM/FM₂/MgO/FM₃ structure, where FM denotes a ferromagnetic layer and NM represents a nonmagnetic spacer layer. FM₂/MgO/FM₃ forms a pMTJ, while FM₂ is antiferromagnetically coupled to FM₁ through the NM spacer, constituting a synthetic antiferromagnet (SAF). This architecture enables the investigation of VCEC by monitoring the effective field induced on the free layer (FM₂) under applied voltage. We demonstrate that the VCEC induces a bipolar effective magnetic field that persists on the nanosecond timescale. Although VCEC theoretically enables bipolar switching,

we focus on antiparallel-to-parallel (AP-to-P) switching, as strong VCMA suppresses the reverse switching by increasing the barrier height in our device. With the assistance of VCMA, AP-to-P switching occurs as fast as 87.5 ps with 50% probability. We further reveal an inverse scaling behavior between voltage amplitude and pulse width around 1 ns, analogous to the super-threshold regime in STT switching, indicating a voltage-induced single-domain precessional switching. We additionally investigate voltage-induced switching behavior through a size-dependent study, revealing that smaller devices exhibit more efficient switching, as confirmed by macrospin simulations. This improvement is attributed to the enhanced dynamic response of the coupled layer in reduced dimensions, corresponding to an increased effective damping behavior of the free layer.

Characterization of the VCEC stack and device properties

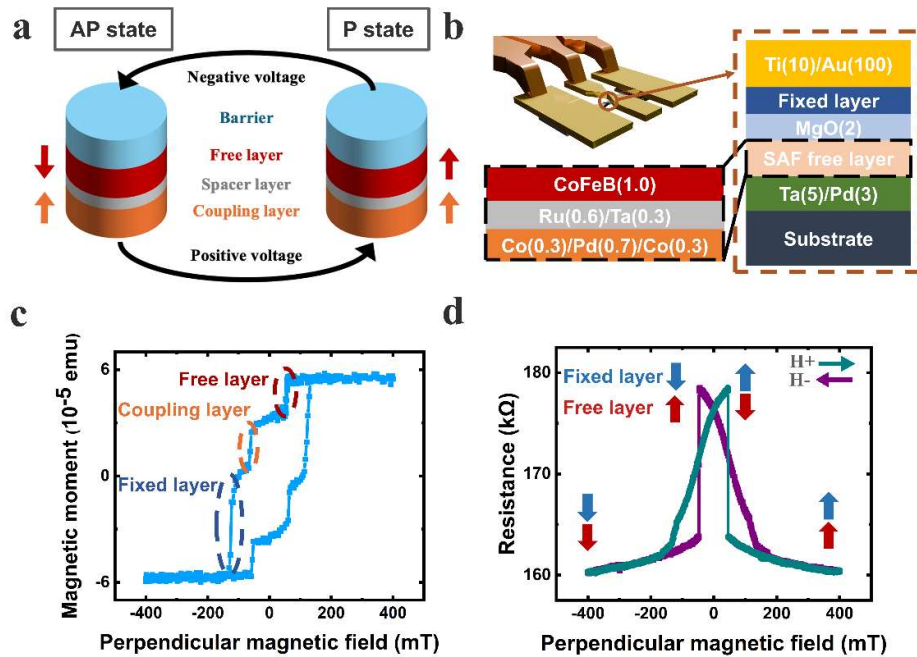


FIG. 1 | Device structure and magnetic properties of the VCEC stack. (a) Schematic illustration of voltage-controlled exchange coupling (VCEC)-induced switching. Under a positive voltage, the AP state is favored, while a negative voltage favors the P state. (b) Schematic of the pMTJ stack structure incorporating a SAF free layer. The top-left inset shows a schematic illustration of a patterned pillar with electrodes configured for GSG probe measurements. (c) Magnetization vs. perpendicular magnetic field loop of the stack after annealing. The sharp switching transitions indicate the presence of perpendicular magnetic anisotropy (PMA) in all magnetic layers. (d) Resistance vs. perpendicular magnetic field major loop of a patterned pMTJ device (500 nm diameter). The clear bistable states confirm preserved PMA in the device after patterning.

Fig. 1a illustrates the fundamental structure enabling the VCEC effect. The free and coupling layers, positioned beneath the barrier layer, are exchange-coupled through the spacer layer. Their relative alignment, either AP or P, can be controlled by applying a negative or positive

voltage. Due to the free layer's lower coercivity, only the free layer switches under the influence of the voltage. It is well established that modulating the spacer layer thickness induces oscillatory coupling between the AP and P states^{46,47}, a characteristic behavior of the Ruderman-Kittel-Kasuya-Yosida (RKKY) interaction. Similarly, modulating the electrostatic potential across the barrier layer can shift the relative energy levels of the AP and P states, enabling voltage-controlled switching^{38,39} (Supplementary Section 1). To experimentally realize this concept, we deposited a multilayer stack on a SiO₂ substrate with the structure (units in nm): Substrate / Ta (5) / Pd (3) / Co (0.3) / Pd (0.7) / Co (0.3) / Ru (0.6) / Ta (0.3) / CoFeB (1) / MgO (2.0) / CoFeB (1.3) / Ta (0.7) / [Pd (0.7)/Co (0.3)]₄ / Pd (5). The core structure, illustrated in Fig. 1b, consists of four functional components: (1) Fixed layer — [CoFeB (1.3) / Ta (0.7) / [Pd (0.7) / Co (0.3)]₄], providing a stable reference magnetization; (2) Free layer — [CoFeB (1)], positioned beneath the MgO barrier, whose magnetization is tunable via voltage; (3) Coupling layer — [Co (0.3) / Pd (0.7) / Co(0.3)], generating the interlayer exchange coupling field; (4) Spacer layer — [Ru (0.6) / Ta (0.3)], mediating the interlayer exchange coupling between the free and coupling layers. A relatively thick MgO barrier (2 nm) was selected to suppress current-driven effects while allowing the application of higher voltages.

After rapid thermal annealing, the PMA of the stack was confirmed by an out-of-plane M–H loop (Fig. 1c) measured using a vibrating sample magnetometer (VSM). The three-step magnetization reversal process, from +400 to -400 mT, corresponds to the sequential switching of the free, coupling, and fixed layers. Switching the free layer before the external field reaches zero indicates the realization of antiferromagnetic (AF) exchange coupling at the zero magnetic field. Pillars of various diameters (100–2000 nm) were fabricated via photolithography and electron-beam lithography (Methods). An oblique schematic of the patterned device and electrode configuration is shown in Fig. 1b. The reduced overlap between the top and bottom electrodes enables efficient high-frequency (>1 GHz) pulse injection via a ground–signal–ground (GSG) probe. Fig. 1d presents the resistance–field (R–H) loop of a 500 nm device, revealing distinct resistance states corresponding to different free layer magnetization orientations. The measured tunneling magnetoresistance (TMR) ratio is approximately 11%, with a resistance–area (RA) product of $3.93 \times 10^4 \Omega \cdot \mu\text{m}^2$. The relatively lower TMR compared to conventional MTJs could be improved by enhancing the MgO quality. This was not further optimized in the present study, as the TMR signal serves solely to monitor the magnetic state for evaluating the VCEC effect. A size-dependent resistance analysis, as detailed in Extended Data Fig. 1b, aligns well with theoretical expectations, confirming that the electrically active pillar size matches the designed device geometry.

VCMA and VCEC revealed by minor loops

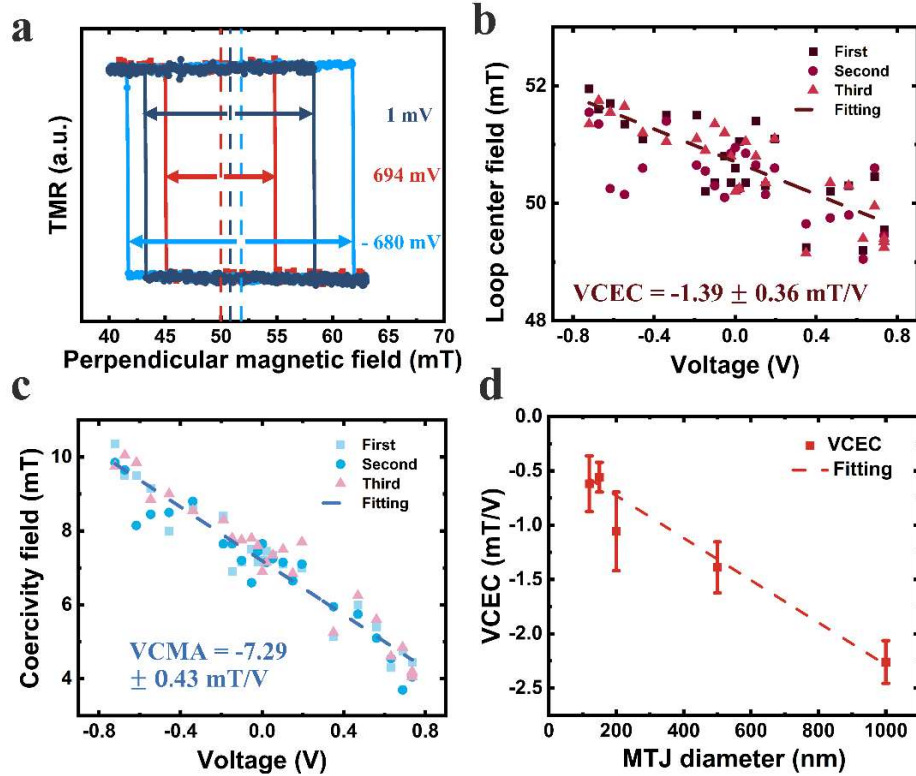


FIG. 2 | Voltage-induced effective fields from VCEC and VCMA. (a) Normalized minor hysteresis loops of a 500 nm MTJ under various applied voltages. Positive (negative) voltages narrow (broaden) the loop width due to VCMA, and shift the loop leftward (rightward) due to VCEC. Voltage dependence of the (b) loop center field and (c) coercivity are extracted from minor loops. For each voltage, three loops are measured to reduce statistical uncertainty. Linear fits to the data yield the VCEC and VCMA coefficients. (d) Extracted VCEC strength as a function of pillar diameter. Error bars represent fitting uncertainties.

Fig. 2a shows normalized electrical minor hysteresis loops of a 500 nm device under different voltages. Before each measurement, a large magnetic field was applied to saturate magnetization along the positive direction, establishing a well-defined initial state where only the free layer's magnetization is reversed in the AP state. A constant current was used to monitor the device resistance, and the average voltage between AP and P states was recorded. Under applied voltage, two distinct effects are expected: VCMA and VCEC. The VCMA effect modifies the PMA of the free layer, altering the coercivity. Specifically, the minor loop becomes wider under negative voltage, consistent with VCMA-induced enhancement of interfacial anisotropy due to electron depletion^{29,30}. In contrast, VCEC manifests as a shift of the minor loop center due to voltage-induced modulation of the exchange coupling field. The loop shifts either left or right, depending on voltage polarity.

To quantify these effects, loop center field and coercivity were extracted by averaging three minor loop measurements per voltage condition. As shown in Fig. 2b,c, both parameters exhibit approximately linear voltage dependence. The extracted VCEC and VCMA strengths, expressed as the effective magnetic field per volt, are -1.39 ± 0.36 mT/V and -7.29 ± 0.43 mT/V, respectively. The significantly smaller magnitude of VCEC compared to VCMA prevents bipolar switching in our devices (Supplementary Section 2). The reduced VCEC strength may stem from limited interlayer coupling or non-uniform voltage distribution across the device structure. Enhancement may be further achieved by optimizing the spacer layer and improving the MgO barrier's crystalline quality.

Importantly, the observed loop shift cannot be attributed to STT, as: (1) it exhibits a linear dependence on the applied voltage, and (2) in STT-driven switching, a positive current favors the AP state, contradicting the observed behavior. Having established the VCEC origin of the loop shift, we next examine how the VCEC strength varies with device size. As shown in Fig. 2d, the extracted VCEC strength decreases with decreasing device diameter, exhibiting an approximately linear relationship. This trend suggests that smaller devices exhibit weaker VCEC effects, likely due to pillar boundary effects, where the intact central area scales as $S/D \sim d$, with S being the pillar area, D the perimeter, and d the pillar diameter. The VCMA strength, expressed as the effective field per volt, does not exhibit a clear size dependence, likely due to the variations in coercivity even among pillars of the same nominal size (Supplementary Section 2). Together, these results establish the presence of the VCEC effect with a clear voltage dependence and predictable size scaling behavior. Building upon these findings, we next investigate whether VCEC can support nanosecond-scale magnetization switching under voltage pulses.

Nanosecond-scale VCEC switching under voltage pulses

To investigate the response of the pMTJ under an ultrafast voltage pulse, we implemented the circuit shown in Fig. 3a. A DC bias current of 5 nA was continuously applied through the DC port of a bias-T to monitor the resistance by measuring the voltage, while ultrafast voltage pulses were injected through the AC port. Since the DC bias current is much smaller than the critical current required for switching, it does not interfere with the magnetization state (Method). Fig. 3b illustrates the testing sequence. A 1 mT out-of-plane magnetic field is initially applied to set the pMTJ to the AP state. The field is then adjusted to the bistable region, where voltage pulses with varying widths and amplitudes are applied. After each pulse, the resistance is measured to determine whether switching has occurred. The cycle is repeated 200 times under each condition to obtain the switching probability.

Fig. 3c shows the minor loop of a 150 nm device, which exhibits relatively larger coercivity and is selected to investigate the effect of an external magnetic field on switching. Magnetic fields ranging from 40 to 48 mT, within the bistable region, are chosen. Under each magnetic field, the voltage amplitude is fixed at 3.56 V, while the pulse width is gradually increased from 0.5 ns until the switching probability approaches approximately 0.9. The corresponding results, shown in Fig. 3d, exhibit an increased switching probability with increasing pulse width

and are well fitted by a sigmoid function. In general, the switching occurred faster as the magnetic field increased from 40 to 48 mT, consistent with the role of a positive applied magnetic field in facilitating AP-to-P switching.

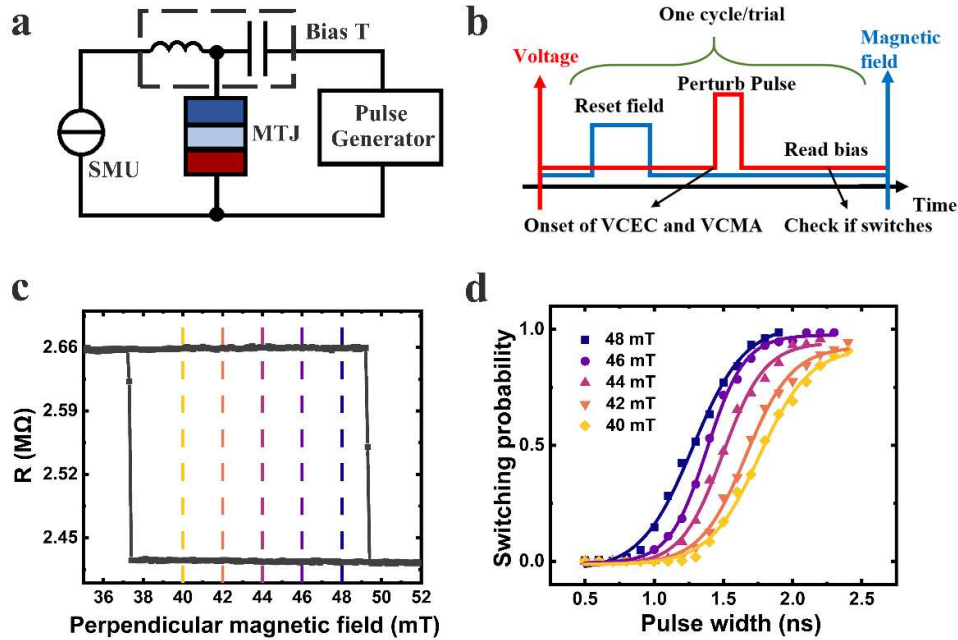


FIG. 3 | Evaluation of VCEC- and VCMA-induced switching using ultrafast pulses. (a) Schematic of the ultrafast pulse switching test setup. A pulse generator delivers voltage pulses to the MTJ, while a source measure unit (SMU) applies a small DC bias and simultaneously monitors the voltage across the device. (b) Test sequence for switching probability measurements. The MTJ is first initialized to the AP state using an external magnetic field. A perturbation voltage pulse from the pulse generator induces VCMA and VCEC effects. A small constant current is applied continuously to monitor the MTJ state after each pulse. (c) Minor hysteresis loop of the 150 nm MTJ. The dashed line marks the external magnetic field used in the switching tests. (d) Switching probability as a function of pulse width, measured at a fixed pulse amplitude of 3.56 V under selected external magnetic fields.

In a device governed solely by the VCMA effect, a positive voltage would contract the minor loop toward the center, and AP-to-P switching would occur only if the applied magnetic field exceeded the loop center field. If the applied magnetic field is below this threshold, AP-to-P switching would be suppressed, as the AP state would be favored. However, the observation of switching events at relatively low magnetic fields of 40 and 42 mT, where VCMA alone would not be sufficient for switching, strongly suggests the involvement of an additional mechanism, namely VCEC, whose effect counteracts the external field and assists AP-to-P magnetization reversal. These findings demonstrate the persistence of the VCEC effect on the nanosecond timescale, excluding any potential contribution of slower ionic drift processes. This further highlights VCEC's potential as a viable replacement for STT in achieving fast, deterministic magnetic switching even in the GHz regime.

Voltage-dependent switching and size effects

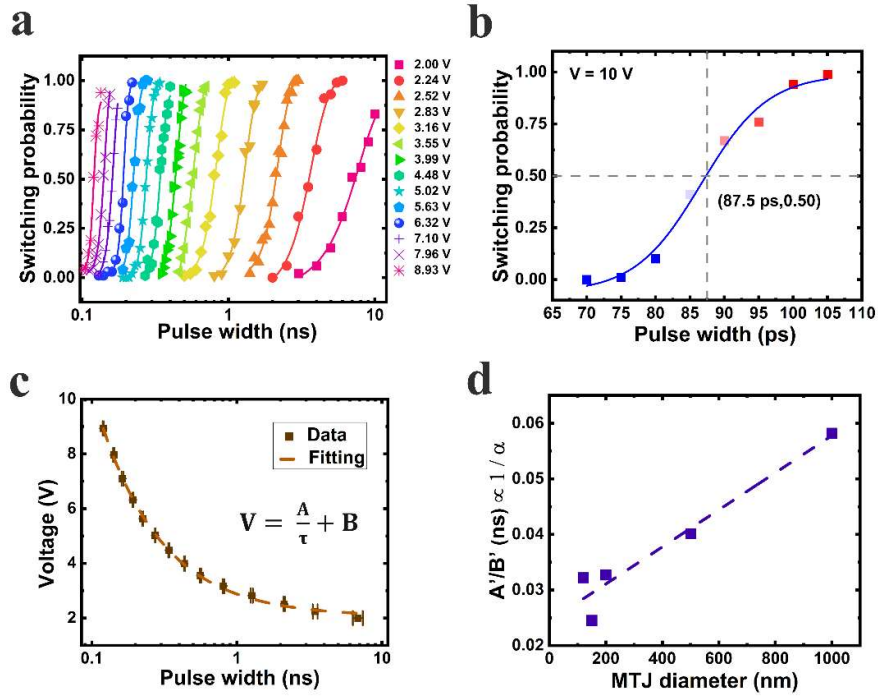


FIG. 4 | Fast switching results under different applied voltages. (a) Switching probability as a function of pulse width under applied voltages ranging from 2.00 V to 8.93 V, with 100 trials per data point. The switching probability increases with pulse width across all voltages, with higher voltages enabling faster switching. (b) Switching probability as a function of pulse width under a fixed 10 V pulse generated by a high-speed pulse generator capable of delivering sub-100 ps pulses, with 100 trials per data point. A 50% switching probability is reached at 87.5 ps, demonstrating ultrafast switching enabled by short, high-voltage pulses. (c) Voltage versus pulse width corresponding to the 50% switching probability points. The data follow an inverse relationship, well captured by the fitting equation shown in the inset. (d) Fitted A/B values as a function of MTJ diameter. In the single-domain model, A/B is inversely proportional to the effective damping constant α , indicating that the damping increases as the device size decreases.

We investigated the effect of voltage amplitude on switching speed under a fixed magnetic field (see Methods). As shown in Fig. 4a, the switching probability increases with pulse width across multiple voltage levels for a 500 nm device, with each curve well fitted by a sigmoid function. The switching is deterministic, with the probability approaching one at longer pulse durations. Higher voltages significantly reduce the critical pulse width required to reach a given switching probability. Reliable switching is observed even at the shortest pulse width of 0.1 ns, which is the minimum supported by the pulse generator (Methods). To further explore the switching speed limit, we employed a second pulse generator with a fixed output of 5 V (resulting in ~ 10 V across the MTJ) and sub-100 ps pulse capability. This setup enabled switching within 87.5 ps of 50% probability, with a 40 ps rise time (Fig. 4b), indicating an

exceptionally short incubation time. The corresponding pulse shape and width are confirmed in Extended Data Fig. 2.

To quantify the observed switching behavior, we extracted the pulse width corresponding to 50% switching probability ($\tau_{50\%}$) and analyzed its dependence on the applied voltage. Fig. 4b shows the extracted $\tau_{50\%}$ values as a function of voltage, where the relationship is well-described by the form: $V = \frac{A}{\tau} + B$. Here, V is the voltage, τ is the pulse width, and A and B are fitting parameters. A similar trend is observed across different device sizes, as shown in Extended Data Fig. 3a. This inverse relationship between voltage and pulse width resembles the super-threshold behavior commonly observed in STT switching, suggesting a single-domain precessional switching mechanism^{48,49}. To further understand the voltage-driven dynamics, we derive an analogous expression for voltage-induced torque based on the single-domain model (Supplementary Section 3). The fitting parameters can be expressed as:

$$A = \frac{\left(\frac{1 + \alpha^2}{\alpha\gamma\mu_0}\right) \cdot \ln\left(\frac{\pi}{2\theta_0}\right)}{|a + b|}, \quad (1)$$

$$B = \frac{H_k - H_{\text{ext}}}{|a + b|}, \quad (2)$$

where α is the Gilbert damping constant, γ is the gyromagnetic ratio, μ_0 is the vacuum permeability, θ_0 is the initial angle of magnetization relative to the easy axis, H_k is the effective anisotropy field, and H_{ext} is the applied magnetic field relative to the loop center field. Parameters a and b represent the effective field coefficients associated with the VCEC and VCMA effects, respectively, each quantified as the effective magnetic field per volt. Notably, B corresponds to the critical voltage required to overcome the energy barrier for switching.

To investigate the size-dependent switching behavior, we analyze the scaling of the extracted fitting parameters A' and B' , which correspond to the numerators of the right-hand-side terms in equations (1) and (2). The variations of A' and B' with device size are plotted in Extended Data Fig. 3. A' generally exhibits an increasing trend with device size, accompanied by minor fluctuations, while B' remains nearly constant with variations that arise from differences in the manually selected applied magnetic field (see Methods). These fluctuations in B' in turn influence A' by modifying the initial magnetization angle θ_0 , following the relation: $A' \propto \frac{1}{\theta_0} \propto$

$H_k - H_{\text{ext}} \propto B'$. To account for this, we plot the ratio A'/B' as a function of device size in Fig. 4d. Given the proportionality: $\frac{A'}{B'} \propto \left(\frac{1+\alpha^2}{\alpha}\right)$ and noting that for $\alpha \ll 1$, this reduces to $\frac{A'}{B'} \propto \left(\frac{1}{\alpha}\right)$.

The observed trend implies that the effective damping constant increases as the device size decreases. This enhanced damping behavior in smaller devices facilitates faster magnetization switching under voltage excitation.

Faster voltage-driven switching by enhanced damping

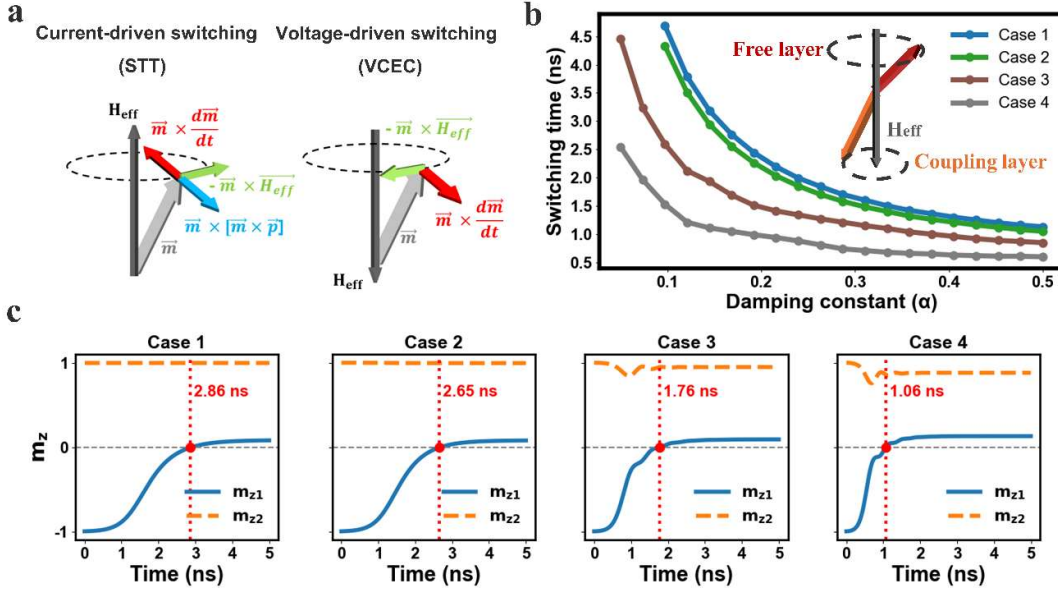


FIG. 5 | Illustration of the torque direction and the simulation result. (a) (left): Torque orientation in STT-induced switching. The anti-damping-like torque must overcome the damping-like torque to induce switching. (a) (right): Torque orientation in voltage-induced switching. The effective field reverses, as does the damping-like torque. The torque drives the local magnetic moment toward the new H_{eff} direction to minimize energy. (b) Simulation results show switching time as a function of the damping constant. Four cases are considered: Case 1: A single free layer. Case 2-4: A coupled system where the free layer interacts with the coupling layer. Specifically, Case 2: $H_{\text{CP}}=50$ mT, $H_{\text{K2}}=500$ mT, Case 3: $H_{\text{CP}}=25$ mT, $H_{\text{K2}}=50$ mT, Case 4: $H_{\text{CP}}=50$ mT, $H_{\text{K2}}=50$ mT. In all cases, a higher damping constant results in shorter switching times. The introduction of coupling accelerates switching, and the trajectory of the coupling layer further influences the magnitude of this effect. (c) Time-resolved normalized z-component of free layer (m_{z1}) and coupling layer (m_{z2}) under 4 cases when $\alpha = 0.16$.

Fig. 5a illustrates the torque directions for STT and VCEC switching. In STT switching (Fig. 5a, left), the spin current primarily exerts an anti-damping-like torque along $\vec{m} \times (\vec{m} \times \vec{p})$ on the local magnetization. Switching occurs only if this torque overcomes the damping-like torque (along $\vec{m} \times \frac{d\vec{m}}{dt}$). To enhance switching efficiency and speed, significant efforts are needed to reduce the damping constant of the ferromagnetic layer. In contrast, in voltage-induced switching (Fig. 5a, right), the applied voltage reverses the sign of the effective magnetic field (\vec{H}_{eff}), causing the magnetization to precess around the new direction. In this case, the damping-like torque (along $\vec{m} \times \frac{d\vec{m}}{dt}$) acts as the driving force for switching. As a result, a larger damping constant becomes desirable for achieving faster switching. To validate this concept, we performed a macrospin simulation to examine how the switching speed varies

with damping. The simulation models voltage-induced switching at $V = 4$ V for a 500 nm device, consistent with the experimental conditions (Supplementary Section 5). The simulated trajectories of the free layer's normalized magnetic moment under selected damping constants are shown in Extended Data Fig. 5,6 (Case 1), and the corresponding switching times are plotted in Fig. 5b. The results indicate that the switching speed increases with increasing α (for $\alpha < 1$). However, as observed experimentally, achieving sub-nanosecond switching at the same voltage would require an exceptionally high damping constant. Additionally, the experimentally extracted size-dependent variation in α (Fig. 4c) is unexpected, as all devices are patterned from the same material stack and thus should share the same intrinsic α . This discrepancy motivates further investigation into the physical origins of the size effect on switching dynamics.

Although the macrospin simulations described above assume a rigid coupling layer, this simplification does not fully capture the dynamics of the exchange-coupled system. To address this, we conducted additional simulations incorporating coupled magnetization dynamics under varying interlayer coupling strength (H_{CP}) and coupling layer PMA (H_{k2}), while keeping the effective magnetic field sensed by the free layer constant, as defined in Cases 2–4. In Case 2, we applied $H_{CP} = 50$ mT and set H_{k2} to a large, nonphysical value of 500 mT to suppress the rotation of the coupling layer magnetization. A similar simulation under different α was performed and the results are shown in Fig. 5b. Even under this near-rigid condition, the switching time was slightly shorter than in Case 1. In Case 4, using experimentally relevant values ($H_{CP} = 50$ mT, $H_{k2} = 50$ mT), the switching speed further increased. To investigate the effect of H_{CP} , we reduced it to 25 mT in Case 3 while keeping $H_{k2} = 50$ mT. The switching in this case was slower than in Case 4, but remained faster than in Cases 1 and 2.

The trajectory of the free and coupling layers under different damping values (α) are shown in Extended Data Fig. 5,6. As an example, Fig. 5c summarizes the results for $\alpha = 0.16$ across all four cases. The m_z component switches from -1 to a value above 0, and the moment it crosses zero is defined as the switching time. From Case 1 to Case 4, the deviation of the coupling layer from the out-of-plane direction increases progressively, and the switching speed increases correspondingly. These results reveal a clear dependence of switching speed on the dynamical response of the coupling layer. The simulation trend aligns with our observation that smaller MTJs appear to switch faster. This could be related to the reduced thermal stability in the coupling layer of smaller devices, which may enhance their sensitivity to dynamic excitation during switching. While our simulations capture the role of coupled magnetization dynamics, additional effects such as spin pumping, which is omitted in the model, may further enhance the effective damping and thus help explain the experimental fast switching speed^{50–52}.

Overall, a larger H_{CP} and a smaller H_{k2} facilitate faster switching by increasing the deviation of the coupling layer magnetization during the free layer switching. Such properties are not only favorable for device scaling but also advantageous for ideal bipolar VCEC switching, where the voltage-induced exchange field is sufficiently strong. During the switching process, the strengthened coupling promotes a more pronounced deviation of the coupling layer

magnetization, which enhances the effective damping of the free layer and thus accelerates magnetization reversal.

Conclusions

In summary, we demonstrate that VCEC induces a bipolar effective magnetic field, which persists under nanosecond-scale voltage pulses. These results provide direct experimental evidences that exchange coupling can be modulated electronically, distinguishing VCEC from magneto-ionic mechanisms that rely on ionic migration. By combining VCEC with VCMA, we achieve deterministic switching within 87.5 ps at 50% probability, highlighting the ultrafast operation potential of voltage-driven MTJs. Furthermore, by varying the applied voltage and device size, we observe an inverse relationship between voltage and switching time, as well as a pronounced size-dependent switching behavior. Macrospin modeling indicates that the torque responsible for voltage-driven switching is field-like, in contrast to the damping-like torque of STT and SOT mechanisms. This field-like torque benefits from enhanced angular momentum dissipation via exchange coupling, leading to accelerated magnetization relaxation. Simulations further support this interpretation by revealing a clear correlation between switching speed and dynamic perturbations of the coupling layer during reversal. Based on these insights, even faster switching is anticipated in bipolar-switchable VCEC-MTJs, not only due to the increased effective magnetic field but also as a result of the more pronounced dynamic response of the coupling layer under stronger interlayer coupling. Together, these findings establish VCEC as a fast, deterministic, and energy-efficient voltage-driven switching mechanism. Further engineering of device structures and material interfaces may unlock even greater performances, paving the way toward high-speed, low-power spintronic memory and logic technologies.

References

1. Wang, J.-P. *et al.* A Pathway to Enable Exponential Scaling for the Beyond-CMOS Era: Invited. in *Proceedings of the 54th Annual Design Automation Conference 2017* 1–6 (Association for Computing Machinery, New York, NY, USA, 2017).
doi:10.1145/3061639.3072942.
2. Guo, Z. *et al.* Spintronics for Energy- Efficient Computing: An Overview and Outlook. *Proceedings of the IEEE* **109**, 1398–1417 (2021).
3. Puebla, J., Kim, J., Kondou, K. & Otani, Y. Spintronic devices for energy-efficient data storage and energy harvesting. *Commun Mater* **1**, 1–9 (2020).

4. Saida, D. *et al.* Low-Current High-Speed Spin-Transfer Switching in a Perpendicular Magnetic Tunnel Junction for Cache Memory in Mobile Processors. *IEEE Transactions on Magnetics* **50**, 1–5 (2014).
5. Kitagawa, E. *et al.* Impact of ultra low power and fast write operation of advanced perpendicular MTJ on power reduction for high-performance mobile CPU. in *2012 International Electron Devices Meeting* 29.4.1-29.4.4 (2012).
doi:10.1109/IEDM.2012.6479129.
6. Worledge, D. C. Spin-Transfer-Torque MRAM: the Next Revolution in Memory. in *2022 IEEE International Memory Workshop (IMW)* 1–4 (2022).
doi:10.1109/IMW52921.2022.9779288.
7. Kawahara, T., Ito, K., Takemura, R. & Ohno, H. Spin-transfer torque RAM technology: Review and prospect. *Microelectronics Reliability* **52**, 613–627 (2012).
8. Worledge, D. C. & Hu, G. Spin-transfer torque magnetoresistive random access memory technology status and future directions. *Nat Rev Electr Eng* **1**, 730–747 (2024).
9. Cai, H. *et al.* A survey of in-spin transfer torque MRAM computing. *Sci. China Inf. Sci.* **64**, 160402 (2021).
10. Cui, Y.-T. *et al.* Single-Shot Time-Domain Studies of Spin-Torque-Driven Switching in Magnetic Tunnel Junctions. *Phys. Rev. Lett.* **104**, 097201 (2010).
11. Devolder, T. *et al.* Time-resolved spin-torque switching in MgO-based perpendicularly magnetized tunnel junctions. *Phys. Rev. B* **93**, 024420 (2016).

12. Krivorotov, I. N. *et al.* Time-Domain Measurements of Nanomagnet Dynamics Driven by Spin-Transfer Torques. *Science* **307**, 228–231 (2005).
13. Yang, Q. *et al.* Field-free spin–orbit torque switching in ferromagnetic trilayers at sub-ns timescales. *Nat Commun* **15**, 1814 (2024).
14. Lyu, D. *et al.* Sub-ns Switching and Cryogenic-Temperature Performance of Mo-Based Perpendicular Magnetic Tunnel Junctions. *IEEE Electron Device Lett.* **43**, 1215–1218 (2022).
15. Lyu, D. *et al.* Electrical control of the switching layer in perpendicular magnetic tunnel junctions with atomically thin Ir dusting. *Applied Physics Letters* **124**, 182401 (2024).
16. Safranski, C. *et al.* Reliable Sub-nanosecond MRAM with Double Spin-torque Magnetic Tunnel Junctions. in *2022 IEEE Symposium on VLSI Technology and Circuits (VLSI Technology and Circuits)* 288–289 (2022).
doi:10.1109/VLSITechnologyandCir46769.2022.9830306.
17. Hu, G. *et al.* Double spin-torque magnetic tunnel junction devices for last-level cache applications. in *2022 International Electron Devices Meeting (IEDM)* 10.2.1-10.2.4 (2022). doi:10.1109/IEDM45625.2022.10019402.
18. Hu, G. *et al.* 2X reduction of STT-MRAM switching current using double spin-torque magnetic tunnel junction. in *2021 IEEE International Electron Devices Meeting (IEDM)* 2.5.1-2.5.4 (2021). doi:10.1109/IEDM19574.2021.9720691.

19. Pruckner, B., Fiorentini, S., Goes, W., Selberherr, S. & Sverdllov, V. Micromagnetic modeling of double spin-torque magnetic tunnel junction devices. *Physica B: Condensed Matter* **688**, 416124 (2024).
20. Kent, A. D., Özyilmaz, B. & del Barco, E. Spin-transfer-induced precessional magnetization reversal. *Applied Physics Letters* **84**, 3897–3899 (2004).
21. Díaz, E. *et al.* Energy-efficient picosecond spin-orbit torque magnetization switching in ferro- and ferrimagnetic films. *Nat. Nanotechnol.* **20**, 36–42 (2025).
22. Jhuria, K. *et al.* Spin-orbit torque switching of a ferromagnet with picosecond electrical pulses. *Nat Electron* **3**, 680–686 (2020).
23. Polley, D. *et al.* Picosecond spin-orbit torque-induced coherent magnetization switching in a ferromagnet. *Science Advances* **9**, eadh5562 (2023).
24. Park, J., Rowlands, G. E., Lee, O. J., Ralph, D. C. & Buhrman, R. A. Macrospin modeling of sub-ns pulse switching of perpendicularly magnetized free layer via spin-orbit torques for cryogenic memory applications. *Applied Physics Letters* **105**, 102404 (2014).
25. Wu, Y. *et al.* Spin-orbit torque-induced magnetization switching in Pt/Co–Tb/Ta structures. *Applied Physics Letters* **118**, 022401 (2021).
26. Zeng, X. *et al.* Experimental observation and micromagnetic understanding of the current-induced magnetization reversal process in Ta/Pt/[Co/Ni]_nCo/Ta multilayers. *J. Phys. D: Appl. Phys.* **54**, 475001 (2021).
27. Yang, Y. *et al.* Giant spin Hall effect with multi-directional spin components in Ni₄W. Preprint at <https://doi.org/10.48550/arXiv.2411.05682> (2024).

28. Yang, Y. *et al.* Coexistence of unconventional spin Hall effect and antisymmetric planar Hall effect in IrO₂. *Applied Physics Letters* **126**, (2025).
29. Wang, W.-G., Li, M., Hageman, S. & Chien, C. L. Electric-field-assisted switching in magnetic tunnel junctions. *Nature Mater* **11**, 64–68 (2012).
30. Chen, Y.-C. *et al.* Enhanced Voltage-Controlled Magnetic Anisotropy and Field-Free Magnetization Switching Achieved with High Work Function and Opposite Spin Hall Angles in W/Pt/W SOT Tri-Layers. *Advanced Functional Materials* **n/a**, 2416570.
31. Shao, Y. *et al.* Sub-volt switching of nanoscale voltage-controlled perpendicular magnetic tunnel junctions. *Commun Mater* **3**, 1–8 (2022).
32. One, R.-A. *et al.* Route towards efficient magnetization reversal driven by voltage control of magnetic anisotropy. *Sci Rep* **11**, 8801 (2021).
33. Yamamoto, T., Matsumoto, R., Nozaki, T., Imamura, H. & Yuasa, S. Developments in voltage-controlled subnanosecond magnetization switching. *Journal of Magnetism and Magnetic Materials* **560**, 169637 (2022).
34. Deng, J., Liang, G. & Gupta, G. Ultrafast and low-energy switching in voltage-controlled elliptical pMTJ. *Sci Rep* **7**, 16562 (2017).
35. Chen, Y.-C. *et al.* Large and Tunable Electron-Depletion-Based Voltage-Controlled Magnetic Anisotropy in the CoFeB/MgO System via Work-Function-Engineered Pt_xW_{1-x} Underlayers. *ACS Nano* (2025) doi:10.1021/acsnano.5c01956.
36. Yang, Q. *et al.* Ionic liquid gating control of RKKY interaction in FeCoB/Ru/FeCoB and (Pt/Co)₂/Ru/(Co/Pt)₂ multilayers. *Nat Commun* **9**, 991 (2018).

37. Kossak, A. E., Huang, M., Reddy, P., Wolf, D. & Beach, G. S. D. Voltage control of magnetic order in RKKY coupled multilayers. *Sci Adv* **9**, eadd0548 (2023).
38. Bruno, P. Theory of interlayer magnetic coupling. *Phys. Rev. B* **52**, 411–439 (1995).
39. Zhang, D. *et al.* Bipolar Electric-Field Switching of Perpendicular Magnetic Tunnel Junctions through Voltage-Controlled Exchange Coupling. *Nano Lett.* **22**, 622–629 (2022).
40. Zink, B. R. *et al.* Ultralow Current Switching of Synthetic-Antiferromagnetic Magnetic Tunnel Junctions Via Electric-Field Assisted by Spin–Orbit Torque. *Advanced Electronic Materials* **8**, 2200382 (2022).
41. Lyu, D. *et al.* Ferromagnetic resonance and magnetization switching characteristics of perpendicular magnetic tunnel junctions with synthetic antiferromagnetic free layers. *Applied Physics Letters* **120**, 012404 (2022).
42. Surampalli, A. *et al.* Voltage Controlled Interlayer Exchange Coupling and Magnetic Anisotropy Effects in Perpendicular Magnetic Heterostructures. *Advanced Functional Materials* **34**, 2408599 (2024).
43. Tong, Z., Wang, X., Wu, X., Zhang, Y. & Shao, Q. Modeling of Magnetic Tunnel Junction Switching by Voltage-Controlled Exchange Coupling. *IEEE Electron Device Letters* **45**, 1449–1452 (2024).
44. Lyu, D. *et al.* L10 FePd-based perpendicular magnetic tunnel junctions with 65% tunnel magnetoresistance and ultralow switching current density. *AIP Advances* **14**, 025019 (2024).

45. Jia, Q. *et al.* Energy Efficient Stochastic Signal Manipulation in Superparamagnetic Tunnel Junctions via Voltage-Controlled Exchange Coupling. Preprint at <https://doi.org/10.48550/arXiv.2412.06256> (2024).
46. Slonczewski, J. C. Overview of interlayer exchange theory. *Journal of Magnetism and Magnetic Materials* **150**, 13–24 (1995).
47. Parkin, S. S. P. & Mauri, D. Spin engineering: Direct determination of the Ruderman-Kittel-Kasuya-Yosida far-field range function in ruthenium. *Phys. Rev. B* **44**, 7131–7134 (1991).
48. Sun, J. Z. Spin-transfer torque switched magnetic tunnel junction for memory technologies. *Journal of Magnetism and Magnetic Materials* **559**, 169479 (2022).
49. Liu, H. *et al.* Dynamics of spin torque switching in all-perpendicular spin valve nanopillars. *Journal of Magnetism and Magnetic Materials* **358–359**, 233–258 (2014).
50. Heinrich, B. *et al.* Dynamic Exchange Coupling in Magnetic Bilayers. *Phys. Rev. Lett.* **90**, 187601 (2003).
51. Tserkovnyak, Y., Brataas, A. & Bauer, G. E. W. Dynamic exchange coupling and Gilbert damping in magnetic multilayers (invited). *Journal of Applied Physics* **93**, 7534–7538 (2003).
52. Pervez, M. A. *et al.* Damping in synthetic antiferromagnets. *Journal of Magnetism and Magnetic Materials* **548**, 168923 (2022).

Methods

Device fabrication and film growth

The pMTJ stack was deposited on a thermally oxidized Si substrate at room temperature using DC and RF magnetron sputtering in the Shamrock system. The base pressure during deposition was maintained at $< 5 \times 10^{-8}$ Torr. The layer structure of the fabricated stack is as follows (thicknesses in nm): Ta(5) / Pd(3) / Co(0.3) / Pd(0.7) / Co(0.3) / Ru(0.6) / Ta(0.3) / CoFeB(1) / MgO(2.0) / CoFeB(1.3) / Ta(0.7) / [Pd(0.7) / Co(0.3)]₄ / Pd(5). RTP-600S Rapid Thermal Processing System was used for the rapid thermal annealing (RTA) at the temperature of 350°C for 20 min to develop perpendicular magnetic anisotropy (PMA). The magnetic properties of the film stacks were characterized using a vibrating sample magnetometer (VSM) in a Dynacool chamber (Quantum Design). Thin films were patterned into circularly shaped MTJ devices with diameters of 100, 120, 150, 200, 500, 1000, and 2000 nm using electron-beam lithography (EBL) and argon (Ar) ion-beam milling. The electrical size of the devices was validated through the size-dependent resistance. The extracted large resistance-area (RA) product of around $3.93 \times 10^4 \Omega \cdot \mu\text{m}^2$ showed good agreement with the thick MgO thickness of 2 nm.

Electrical measurements

DC electrical measurements were performed using a Keithley 2400 multimeter. Resistance-field (R-H) loops and minor loops were measured at varying applied currents. The currents are converted to the average voltage between AP and P states for voltage effect evaluation. To investigate the response time of VCEC-induced switching, we applied ultrafast voltage pulses to the MTJ using two pulse generators. The setup included a bias-tee circuit to enable simultaneous DC bias application and high-speed pulse injection (Fig. 3a). Model 5541A Bias Tee (80 kHz – 26 GHz, 8 ps rise time) was used. Given that the MTJ resistance is significantly higher than 50 Ω , the actual pulse amplitude at the MTJ approximately doubles according to $\Gamma(R) = 2Z_0 / (Z_0 + R)$, where $R = 50 \Omega$ and Z_0 is dominated by the MTJ impedance, which is much higher than 50 Ω . Generator 1: Picosecond Pulse Labs Pulse Generator 10,060A with the pulse width: 100 ps–10 ns, output voltage: 10 V, max rise time: 55 ps. Generator 2: Alnair Labs Electrical Pulse Generator (EPG-210B-0300-S-P-T-A) with the pulse width: 30 ps – 230 ps, output voltage: 5 V, rise time: 40 ps. All the switching results except for those shown in Fig. 4b are collected by Generator 1. The output pulse profiles in Extended Data Fig. 2 are collected by Tektronix DPO72004B digital phosphor oscilloscope with a bandwidth of up to 20 GHz. For measurement with the fixed magnetic field, the external field was fixed near the AP-to-P switching threshold magnetic field but remained stable enough to prevent spontaneous switching. Each minor loop measurement was repeated 100 times (2 Oe/s) per device to precisely extract the AP-to-P switching field. A field with zero spontaneous switching probability was chosen to ensure that all observed switching was induced by the applied voltage pulse rather than thermal agitation. Switching probability is calculated based on 100 trials for those tests in Fig. 4.

Data availability

Data are available from the corresponding authors upon request.

Code availability

The codes used for the macrospin simulations are available from the corresponding authors upon request.

Acknowledgements

This work was partly supported by the Defense Advanced Research Projects Agency (DARPA) (Advanced MTJs for computation in and near random access memory) under Grant HR001117S0056-FP-042, the Global Research Collaboration (GRC) Logic and Memory program, sponsored by SRC and NSF ASCENT program TUNA: No. 2230963. Authors thank the useful discussion and support from Denis Tonini and Yu Han Huang, a visiting student from National Yang Ming Chiao Tung University, Taiwan. Parts of this work were carried out in the Characterization Facility, University of Minnesota, which receives partial support from the NSF through the MRSEC (Award Number DMR-2011401) and the NNCI (Award Number ECCS-2025124) programs. Portions of this work were conducted in the Minnesota Nano Center, which is supported by the National Science Foundation through the NNCI under Award Number ECCS-2025124. This research also is partially based upon work supported by the National Science Foundation Graduate Research Fellowship under Grant No. 2237827

Author contributions

Q.J. and J.P. designed the experiments. J.P. led and coordinated the research and the manuscript drafting. D.Z. deposited the films. Q.J., B.D., and D.L. performed the annealing. Q.J., Y.C.C., and O.B. fabricated the samples. Q.J. and S.L. conducted the DC electrical and magnetic measurements. Q.J., Y.L., and B.Z. performed the MTJ fast switching test. Q.J. carried out the micromagnetic simulation. Q.J., Y.Y. analyzed the results. Q.J. drafted the first version of the manuscript with input from all authors.

Competing interests

The authors declare no competing interests.

Additional information

Extended data

Supplementary information